Published in final edited form as:
Cell Host Microbe. 2013 February 13; 13(2): 155–168. doi:10.1016/j.chom.2013.01.004.

Anatomically restricted synergistic anti-viral activities of innate and adaptive immune cells in the skin

Heather D. Hickman[1], **Glennys V. Reynoso**[1], **Barbara F. Ngudiankama**[1], **Erica J. Rubin**[1], **Javier G. Magadán**[1], **Stephanie S. Cush**[1], **James Gibbs**[1], **Barbara Molon**[2], **Vincenzo Bronte**[3], **Jack R. Bennink**[1], and **Jonathan W. Yewdell**[1]

[1]Laboratory of Viral Diseases, National Institutes of Allergy and Infectious Diseases, National Institutes of Health, Bethesda, MD 20892

[2]Istituto Oncologico Veneto, Istituto di Ricovero e Cura a Carattere Scientifico (IRCCS), 35128 Padua, Italy

[3]Department of Pathology and Verona University Hospital, Immunology Section, 37134, Verona, Italy

SUMMARY

Despite extensive *ex vivo* investigation, the spatiotemporal organization of immune cells interacting with virus-infected cells in tissues remains uncertain. To address this, we used intravital multiphoton microscopy to visualize immune cell interactions with virus-infected cells following epicutaneous vaccinia virus (VV) infection of mice. VV infects keratinocytes in epidermal foci, and numerous migratory dermal inflammatory monocytes outlying the foci. We observed $Ly6G^+$ innate immune cells infiltrating and controlling foci, while $CD8^+$ T cells remained on the periphery killing infected monocytes. Most antigen-specific $CD8^+$ T cells in the skin did not interact with virus-infected cells. Blocking the generation of reactive nitrogen species relocated $CD8^+$ T cells into foci, modestly reducing viral titers. Depletion of $Ly6G^+$ and $CD8^+$ cells dramatically increased viral titers, consistent with their synergistic but spatially segregated viral clearance activities. These findings highlight previously unappreciated differences in the anatomic specialization of antiviral immune cell subsets.

INTRODUCTION

Skin presents a formidable barrier to pathogen invasion and many viruses require a breach in the epithelium to establish infection. Some orthopoxviruses, including vaccinia virus (VV), circumvent this problem by infecting epidermal keratinocytes (Moss, 2001), a feature which Jenner famously exploited by epicutaneously (ec.) infecting patients. Inoculation of virtually the entire human population with VV resulted in the eradication of smallpox, by many measures the most dangerous of all human pathogens (Fenner, 1988). While many factors contributed to smallpox eradication, ec. inoculation induces a unique immune response poorly matched by other routes (Liu et al., 2010). Indeed, skin scarification is essential for the generation of tissue resident memory $CD8^+$ T cells that protect against subsequent poxvirus infection (Jiang et al., 2012).

Correspondence to Jonathan W. Yewdell, jyewdell@mail.nih.gov.

Due to intense interest in poxviruses as a standard for successful vaccines, a vector for new vaccines (Sutter and Moss, 1992), or potential bioterror agents (Lane et al., 2001), the $CD8^+$ T cell response to VV has been remarkably well characterized. VV peptides recognized by human or mouse $CD8^+$ T cells have been identified (Moutaftsi et al., 2006; Tscharke et al., 2005; Tscharke et al., 2006), leading to definition of robust immunodominance hierarchies of $CD8^+$ T cells responding to individual viral peptides (Flesch et al., 2010; Tscharke et al., 2005; Tscharke et al., 2006; Yewdell, 2006). Knockout mice have revealed gene products governing the strength of the VV-specific $CD8^+$ T cell response ((Remakus and Sigal, 2011; Salek-Ardakani et al., 2009; Seedhom et al., 2012; Zhao and Croft, 2012), for examples).

Despite numerous *ex vivo* studies, surprisingly little is known about the stoichiometric and spatiotemporal organization of individual T cells interacting with virus-infected cells *in situ.* Detailed understanding has, in part, been hampered by difficultly visualizing viral infection during the course of a natural replicative cycle *in vivo*. Though live recombinant VV (rVV) and vesicular stomatitis virus (VSV) have been visualized in lymph nodes (LNs) draining subcutaneous injection sites (Hickman et al., 2011; Hickman et al., 2008; Iannacone et al., 2010), neither virus replicates nodally (Hersperger et al., 2012; Simon et al., 2007). Additionally, rVV- and VSV-infected LN cells die due to viral cytopathic effects before naïve T cells achieve full effector functions, precluding their study as $CD8^+$ T cell targets (Hickman et al., 2008). Thus, a critical unresolved question is how $CD8^+$ T cells *physically* eliminate virus-infected cells and ultimately control active sites of viral replication *in situ*.

In the present study, we use both static *ex vivo* and dynamic intravital multiphoton microscopic (MPM) imaging to better understand $CD8^+$ T cell-mediated control of virus replicating in the skin. We find unexpected spatial organization and trafficking of effector $CD8^+$ T cells. Rather than target infected keratinocytes, $CD8^+$ T cells pursue and lyse infected inflammatory monocytes outlying lesions. In a sophisticated orchestration of immune cell subsets, optimal virus clearance is achieved by coordination of physically partitioned $CD8^+$ cells and $Ly6G^+$ innate immune cells.

RESULTS

Visualization of epicutaneous vaccinia virus infection

To image rVV skin infection, we infected B6 mice epicutaneously (ec.) in ear pinnae with the bifurcated needle routinely used for human smallpox vaccination. To optimize the sensitivity and precision of infected cell tracking, we used a rVV expressing an eGFP fusion protein targeted to the nucleus of infected cells (VV-NP-S-eGFP) (Hickman et al., 2011; Hickman et al., 2008; Norbury et al., 2002). In frozen transverse sections of infected ears (Fig. 1A), we detected small numbers of isolated $eGFP^+$ cells as early as 3 days post-infection (d.p.i.) By plaque assay, infected cell numbers peaked at 5 d.p.i., a time when a majority of infected cells were physically located in large epidermal keratinocytic foci (Fig. 1A–B).

To determine the precise location of rVV-infected cells in epidermal foci, we stained for keratins present in different layers of the epidermis (illustrated in Fig. 1C (reviewed in (Freedberg et al., 2001)). Staining with keratin 10 localized infection to the suprabasal layers of the epidermis (Fig. 1D), which was confirmed by location and lack of staining with the basal cell marker keratin 5 (Fig. 1E). rVV infection induced keratin 6 expression (Fig. 1F), which is synthesized by hyperproliferative keratinocytes during wound healing ((Navarro et al., 1995; Weiss et al., 1984)).

We next examined ec. infected ears using multiphoton microscopy (MPM) (Fig. 1G), distinguishing the dermis by collagen expression (detected via second harmonic excitation

(Li et al., 2012)). Paralleling plaque assays, $eGFP^+$ infected cells were detected in the dermis at 1 d.p.i. and accumulated in number before the appearance of the large keratinocytic foci. By 10 d.p.i., we no longer detected infected cells in most mice. Thus, MPM detects ec. rVV infection of both dermal cells and epidermal keratinocytes.

Migratory inflammatory macrophages are infected by VV

Though MPM imaging studies have yet to report mobile virus-infected cells (Hickman et al., 2011; Hickman et al., 2008; Iannacone et al., 2010; Junt et al., 2007), migratory cells likely play important roles in initiating antiviral responses (Bedoui et al., 2009). MPM imaging over short time periods (30 min. to 2 h.) revealed many motile $eGFP^+$ dermal cells (Fig. 2A and Movie S1). Flow cytometry of cells isolated from ears 5 d.p.i. revealed numerous infected ($eGFP^+$) $CD45^+$ leukocytes, a majority of which (~75%) were $CD11b^+$ $GR\text{-}1^{int}$ inflammatory monocytes (fully characterized as $CD45^+$ $CD11b^+$ $GR\text{-}1^{int}$ $LY6G^-$ $F4/80^-$ $CD11c^-$ cells (Fig. 2B)). Inflammatory monocytes represent the prevalent infected skin leukocyte over the infection course peaking 4–5 d.p.i. before greatly decreasing in number on day 6 (Fig. 2C). Of note, we also identified minor populations of $eGFP^+$ dendritic cells (DCs) and $Ly6G^+$ cells (neutrophils and recently defined $Ly6G^+$ monocytes (Fischer et al., 2011)) (Fig. 2C and S1).

Via MPM, many of the infected dermal cells appeared just outside major keratinocytic foci. Immunohistology of frozen sections revealed that outlying infected cells expressed CD11b (Fig. 2D), consistent with a macrophage lineage. As expected, MPM imaging revealed that infected cells in large epidermal keratinocytic foci were essentially sessile, with average speeds <1 μm/min (Fig. 2E–F and Movie S1). Many infected cells outlying major lesions were motile, however, with an overall average speed of >2 μm/min (Fig. 2F). Motile infected cells, (defined as cells with average speeds >4 SD from cells in foci), exhibited average speeds of ~4 μm/min, similar to a moderately motile lymph node cell (Lindquist et al., 2004).

To further examine the mobility of infected inflammatory monocytes, we imaged LysM-eGFP mice (with green myelomonocytes (monocytes, macrophages, and neutrophils) (Faust et al., 2000)) infected with a rVV expressing blue fluorescent protein (VV-BFP-Ub-S (VV-BFP-ubiquitin-SIINFEKL, as described in (Lev et al., 2010), pseudocolored magenta) (Fig. 2G and Movie S1). This revealed many motile $eGFP^+$ cells (myelomonocytes) that were also BFP^+ (infected with rVV). To determine if these cells were productively infected (able to generate infectious virus progeny), we sorted $CD45^+$ $eGFP^+$ cells from collagenase digested ears 5 d.p.i. and performed plaque assays (Fig. 2H–J). At peak infection, we estimated 3×10^5 infected inflammatory monocytes per ear, from which we recovered 6.5×10^5 pfu of virus (Fig. 2I). In contrast, virus was not recovered from $eGFP^-$ $CD45^+$ cells from the same ears. Comparison to the virus isolated from the total cell population (including keratinocytes) before sorting revealed that inflammatory monocyte-produced virus accounted for ~ 7% of the virus recovered 5 d.p.i. (Fig. 2J). Together, these data indicate that VV productively infects numerous $GR\text{-}1^{int}$ inflammatory monocytes that surround keratinocytic foci and that these highly motile cells produce infectious virus.

Uninfected inflammatory monocytes rapidly respond to rVV infection

Skin injury or infection induces migration of circulating blood neutrophils, monocytes and eventually lymphocytes to the inflammation site (Werner and Grose, 2003). Flow cytometry of dissociated ear revealed most infiltrating cells were inflammatory monocytes (Fig. 3A). Based on expression of the rVV-reporter gene, most inflammatory monocytes in the skin were uninfected, with approximately 10% peak eGFP expression (Fig. 3B).

Immunohistology of frozen sections revealed elevated numbers of $CD11b^+$ cells adjacent to infected cells, penetrating dense infected keratinocytic lesions 5 d.p.i. (Fig. 3C).

We again used LysM-eGFP mice ($eGFP^+$ myelomonocytes) infected with a BFP-expressing rVV (VV-NP-S-BFP, pseudocolored magenta) to identify rVV-infected cells by MPM (Fig. 3D). High numbers of motile, uninfected $eGFP^+$ cells accumulated at the infection site rapidly post-infection (Movie S2). By 4–5 d.p.i., uninfected $eGFP^+$ cells had invaded viral lesions (Fig. 3D–E). Immunohistology showed that lesion-infiltrating cells expressed both GR-1 and Ly6G (Fig 3F), indicating that these cells were not canonical GR-1^{int} $LY6G^-$ inflammatory monocytes but rather either $Ly6G^+$ monocytes (Fischer et al., 2011) or neutrophils. While their late appearance and slower motility than typical neutrophils (Chtanova et al., 2008) would be consistent with $LY6G^+$ monocytes, caution dictates that we refer to them henceforth as $Ly6G^+$ cells. Treatment of mice with a depleting anti-Ly6G Ab resulted in lesions devoid of $eGFP^+$ cellular infiltration, yet clearly spared many outlying $eGFP^+$ cells (Fig. 3H). Thus, both inflammatory monocytes and $Ly6G^+$ cells respond vigorously to ec. infection, with $Ly6G^+$ cells penetrating epidermal lesions.

What is the function of infiltrating cells during rVV infection? Both monocytes and neutrophils can produce reactive oxygen and nitrogen species (ROS and RNS, respectively) at sites of inflammation (Babior, 2004; Halliwell, 2006). To determine which infiltrating cells produced ROS, we isolated cells 5 d.p.i. and treated with a cell-permeant substrate (CellRox) that becomes fluorescent upon oxidation (Fig. 3I). Both inflammatory monocytes and $Ly6G^+$ cells produced ROS, with the highest fluorescence observed in the latter. ROS and RNS can induce cellular, DNA, and protein damage through production of peroxynitrite, a powerful oxidizing and nitrating agent typically detected by the presence of nitrotyrosine (Szabo et al., 2007). Immunohistology of LysM-$eGFP^+$ mice infected with VV-NP-S-BFP with anti-nitrotyrosine Ab revealed intense staining in and around lesions in areas dense with infiltrating $eGFP^+$ cells (myelomonocytes) (Fig. 3J). Importantly, nitrotyrosine staining was eliminated by depletion of GR-1^+ ($Ly6CG^+$) cells, even in heavily infected areas (Fig. 3J). Taken together, these data strongly suggest that infiltrating inflammatory monocytes and $Ly6G^+$ cells produce ROS that eventually leads to protein nitration in and around viral lesions.

$CD8^+$ T cells eliminate infected inflammatory monocytes

$CD8^+$ T cells participate in controlling VV infection after either intraperitoneal (ip.) or intranasal (in.) infection (Moutaftsi et al., 2009; Xu et al., 2004), and long-lasting immunity generated by VV vaccination is $CD8^+$ based (Liu et al., 2010). Therefore, we originally hypothesized that antigen-specific $CD8^+$ T cells would enter keratinocytic lesions and eliminate infected cells.

We analyzed effector $CD8^+$ T cell behavior by adoptively transferring 2 x 10^5 dsRed OT-I TCR transgenic $CD8^+$ T cells (which recognize K^b-SIINFEKL), infecting, and first performing flow cytometry on dissociated ears. OT-I cells appeared 5 d.p.i., plateaued in number 6–7 d.p.i., and decreased on day 8 (Fig. 4A). Surprisingly, MPM revealed that mobile T cells encircled keratinocytic lesions yet did not penetrate, instead moving in paths just outside of the lesions (Fig. 4B–C). Side views of 3D-reconstructions of either MPM or cryosection z-slices revealed that T cells were located in the dermis (blue) surrounding and beneath epidermal lesions on 5–6 d.p.i. (Fig. 4D–E and Movie S3). By 7 d.p.i. most lesions appeared “open” (with a non-fluorescent center) with small numbers of T cells penetrating (Fig. 4D, **bottom panel**). We confirmed the spatial separation of T cells and lesions by transferring dsRed OT-I cells into LysM-eGFP mice and infecting with NP-S-BFP (Fig. S2 and Movie S3). Taken together, these data indicate that $CD8^+$ T cells infrequently infiltrate

large keratinocytic foci, consistent with the idea that $CD8^+$ T cells play only a limited role in clearing virus from these lesions.

Could $CD8^+$ T cells be patrolling the lesion periphery to deal with outlying cells infected by virus emanating from the lesion? MPM revealed that $CD8^+$ T cells actively pursued outlying infected inflammatory monocytes, often extending pseudopodia through tight spaces to contact infected cells (Fig. 4E). In several instances, we imaged $CD8^+$ T cells killing outlying infected cells, generating eGFP-containing cell debris and then retreating (Fig. 4F–G and Movie S3). Using a spot-detection algorithm to further characterize fragments in one instance, a single spot broke into > 6 spots, with diminishing diameter and fluorescence (Fig. 4H). Late 5 d.p.i., with substantial T cells numbers in the skin, most eGFP signal near large lesions was present as cell fragments <5 μm in diameter (compared to 10–15 μm for intact cells), consistent with efficient $CD8^+$ T cell-mediated destruction of virus-infected outlying cells (Movie S3).

To quantitate the participation of $CD8^+$ T cells in eliminating rVV-infected cells outside lesions, we enumerated infected cells at different d.p.i. (Fig. 4I). As before, gating on $CD45^+$ cells (those of hematopoietic origin) revealed ~ 2% of the total leukocytes in the ear were rVV-infected 5 d.p.i. When high numbers of OT-I cells were present in the skin 6 d.p.i., we no longer detected large quantities of $eGFP^+$ infected cells. $CD8^+$ depletion increased numbers of infected cells, while NK depletion had a minor effect (Fig. 4J). Under the same conditions, infection with rVV lacking OT-I cognate Ag (VV-NP-eGFP) increased infected cell numbers relative to infection with VV-NP-S-eGFP (Fig. 4K). This effect was less dramatic, however, than total CD8 depletion, demonstrating a role for endogenous CD8+ T cells in clearing infected leukocytes, but also showing that endogenous responders are limiting at this timepoint.

Taken together, these data indicate that $CD8^+$ T cells are principally responsible for elimination of infected inflammatory monocytes outlying major keratinocytic foci.

Chemokines are induced by VV scarification and localize to viral lesions

How are $CD8^+$ T cells physically excluded from lesions while $Ly6G^+$ cells readily enter? Molon *et al.* (2011) described a similar phenomenon in anti-tumor responses due to chemokine nitration. While monocytes responded to nitrated chemokines and entered tumors, T cells could not. To determine if a similar mechanism occurred after rVV infection, we quantitated temporal chemokine production in the ear using multiplex protein analysis (Fig. 5A). CCL2, a monocyte chemoattractant (reviewed in (Deshmane et al., 2009)), exhibited the largest early increase, consistent with the rapid response of inflammatory monocytes. Levels of T cell-tropic CCR5-ligand chemokines CCL3, CCL4, and CCL5 increased beginning 5 d.p.i., concomitant with T cell entry into the ear. Since we previously reported that CCR5-ligand chemokine expression attracts OT-I $CD8^+$ T cells and partially dictates their location after lymph node rVV-infection (Hickman et al., 2011), we next determined chemokine location in the infected skin. Immunohistology of LysM-$eGFP^+$ ears 5 d.p.i. with VV-NP-S-BFP (Fig. 5B) revealed both CCL3 and CCL5 (and less intense CCL4) staining concentrated in and around rVV lesions. Thus, T cell tropic chemokines are produced after rVV-infection and are found within viral lesions, yet T cells do not enter.

The presence of $eGFP^+$ myelomonocytes producing ROS in the same area as the heaviest chemokine staining suggested possible protein nitration. Thus, we stained sections 5 d.p.i. for both nitrotyrosine (red) and CCL3 (grey) (Fig. 5C). The two stains colocalized intensely inside the lesion and outside lesions to a lesser extent. Calculating the ratio of CCL3 (the CCR5-ligand chemokine with the best immunohistochemical staining) to nitrotyrosine staining revealed that the ratio of CCL3/nitrotyrosine was much higher outside lesions than

within (Fig. 5FD). To quantify this effect, we analyzed ~25 higher magnification images as either lesion- (Fig. 5E) or outlying infected cell- (Fig. 5F) bearing and calculated the CCL3/nitrotyrosine ratio (Fig. 5G). We found a CCL3/nitrotyrosine ratio of 1.06 inside lesions versus 1.95 outside in areas containing infected inflammatory monocytes.

Thus, although nitrotyrosine was present in both areas, unmodified chemokine is favored outside viral lesions. Taken together, these data are consistent with chemokine nitration controlling T cell localization within and around VV lesions.

Peroxynitrite products dictate T cell location during infection

If chemokine nitration (or nitration of any chemoattractant) dictates T cell exclusion from lesions, inhibition of peroxynitrite could result in T cell penetration. To test this, we transferred dsRed OT-I cells into LysM-eGFP mice and infected with VV-NP-S-BFP. Four d.p.i. we treated with a single dose of AT38 ([3-(aminocarbonyl)furoxan-4-yl]methyl salicylate), a potent inhibitor of peroxynitrite generation (Molon et al., 2011). Remarkably, MPM images of AT38-treated mice showed a clear redistribution of T cells into viral lesions (Figure 6A, top panels and Movie S4). Although lesion size at 5 d.p.i. was unaffected by AT38 treatment (Fig. S3), the number of $CD8^+$ T cells within lesion boundaries increased ~3.5-fold (Fig. 6B).

Presumably, relocated T cells could now eliminate previously inaccessible virus-infected keratinocytes. In this case we would predict that lesions would no longer appear as solid spheres of fluorescence, but would instead have dark regions where fluorescent-infected keratinocytes once lurked. Examination of lesion morphology 6 d.p.i. (one day after initial T cell entry) in the presence or absence of AT38 (Fig. 6C–D) revealed that lesions in control mice remained largely in a closed conformation (e.g. no dark center). Significantly more lesions in treated mice were open (dark center) and often discontinuous. Importantly, treatment with AT38 in conjunction with $CD8^+$ T cell depletion eliminated lesion "opening," demonstrating that $CD8^+$ T cells were required for this effect. Consistent with enhanced $CD8^+$ T cell encounters with virus-infected cells inside the lesion, we observed a trend toward elevated numbers of OT-I production of IFN-γ in AT38-treated mice (Fig. 6E).

Next, we visualized $CD8^+$ T cell interactions with infected keratinocytes inside viral lesions after AT38 treatment (Fig. 6F). T cells formed long-lasting interactions with keratinocytes and, in several instances, we observed retreating T cells containing fluorescent keratinocyte fragments, consistent with killing. Moreover, AT38 treatments decreased virus titers 2-fold 6 d.p.i., further consistent with T cell effector function (Fig. 6G). By 7 d.p.i., lesions were naturally opened, and there was no significant difference in AT38- versus vehicle-treated mice (Fig. 6G), providing an internal control for the non-specific effects of AT38 on virus recovery.

Taken together, these data suggest that peroxynitrite products control $CD8^+$ T cell entry into and consequent activity within viral lesions.

$CD8^+$ T cells and $Ly6G^+$ cells synergize to clear ec. virus

The location of $Ly6G^+$ cells within lesions and $CD8^+$ T cells outside lesions suggested specific functions for each cell subset in rVV clearance. As described above, $CD8^+$ T cells eliminate outlying infected inflammatory monocytes (Fig. 4). To examine the role of $CD8^+$ T cells in resolving lesions, we infected mice with rVV, allowed effector T cells to eliminate outlying infected cells (which occurs prior to 6 d.p.i.), then Ab-depleted $CD8^+$ T cells (Fig. 7A). Four days later, we examined and the number and type of lesions in the presence or absence of $CD8^+$ T cells (Fig. 7B). Under both conditions we observed a few remaining lesions with hollow, non-fluorescent centers (open) along with many partially resolved

lesions (disturbed collagen but no remaining fluorescence). Statistically, CD8 depletion had no effect on the number of open, fluorescent lesions (Fig. 7B). Hence, $CD8^+$ T cells are not necessary for viral lesion clearance after the initial elimination of outlying virus-infected inflammatory monocytes.

By contrast, treating mice with anti-Ly6G Ab to deplete lesion-infiltrating $Ly6G^+$ cells delayed clearance of lesions (Fig. 7C), with >80% of 7 d.p.i. lesions remaining in a solidly fluorescent, closed conformation, compared to only ~20% in control mice (Fig. 7D). However, viral titers were only increased ~ 3.25-fold by $Ly6G^+$ cellular depletion (Fig. 7E). Thus, although $Ly6G^+$ monocytes infiltrate lesions and are more efficient at viral clearance than relocated T cells (Fig. 6G), they cannot single-handedly eliminate all infectious virus in the skin.

Since neither $CD8^+$ T cells nor $Ly6G^+$ monocytes alone could control viral infection, we addressed their potential synergism by co-depleting the two cell subsets (Fig. 7F). Co-depletion increased viral titers > 25-fold 7 d.p.i., far greater than depletion of a single cell type. With continued co-depletion, we observed fluorescent lesions (closed, solid) remaining at 14 d.p.i., which we never observed in untreated mice (Fig. 7G). Likewise, co-depleted ears still contained infectious virus at 14 d.p.i., while controls did not (Fig. 7H). Finally, depletion of both cell types resulted in considerable necrosis and pathology in infected ears of Ab-treated mice (Fig. 7I).

Taken together, these data lead to the critical conclusion that a spatially coordinated and synergistic attack of innate and adaptive immune effectors is required to control acute viral infection in the skin.

DISCUSSION

While the contributions of the various immune effector cells to controlling a given viral infection are imperfectly known, it is increasingly clear that $CD8^+$ T cells participate in resolving and/or preventing many infections. This has enhanced enthusiasm for vaccines aimed principally at generating protective $CD8^+$ T cell responses (Nolz and Harty, 2011). Fully harnessing the power of $CD8^+$ T cells for vaccines demands knowledge of the optimal method for eliciting cells that provide the most potent anti-viral effector function at infection sites. In this study, we describe several previously unknown aspects of the $CD8^+$ T cell response to viral infection *in situ*.

Vaccinia virus robustly replicates in the skin when inoculated via scarification, the current and classical route for smallpox vaccination (Moss, 2001; Yirrell et al., 1994). VV-infects both suprabasal epidermal keratinocytes as expected, but also sizable numbers of mobile inflammatory leukocytes recruited to infected keratinocytic lesions (Figs. 1 and 2). Infected inflammatory monocytes produce infectious virus, making them potentially dangerous vehicles for viral dissemination given their high mobility. MPM clearly reveals that $CD8^+$ T cells pursue and eliminate mobile infected cells before they can broadcast virus.

Although the precise kinetics of virus-infected cell killing will require further study, we observed $CD8^+$ T cell lysis of infected inflammatory monocytes minutes after cellular conjugate formation (Movie S3), suggesting that $CD8^+$ T cells are highly efficient at eliminating these cells. Conversely, rather than kill infected keratinocytes, T cells instead patrolled lesion boundaries (Fig. 4). Pharmacological blockade of peroxynitrite generation enabled T cells to enter lesions, where they could eliminate infected keratinocytes (Fig. 6). This demonstrates that T cell entry into lesions is signal-limited, likely due to nitration of chemotactic factors in the highly chemically reactive environment generated by $Ly6G^+$ cells infiltrating into lesions. This exquisite spatial segregation of $CD8^+$ T cells leads to the

surprising conclusion that the majority of Ag-specific anti-viral $CD8^+$ T cells in VV-infected ears do not interact with virus-infected cells, even when the latter exist in high numbers. Ergo, simply counting the local $CD8^+$ T cell response is insufficient to gauge the effectiveness of the response, since it ignores anatomic complexities that limit $CD8^+$ T cell anti-viral activity.

Why would the immune system segregate antiviral effectors? Perhaps this allows $CD8^+$ T cells to focus on mobile infected cells that might escape immune clearance without dallying with infected cells that can be controlled via other means. Alternatively, $CD8^+$ T cells may be dysfunctional/destroyed in the lesion interior in the presence of high levels of ROS/RNS, while monocytes can better handle the chemical stress that they themselves generate.

Although many important questions remain regarding the participation of other innate and adaptive immune cells in resolving peripheral infections and repairing damaged tissues, our findings provide a template for understanding the anatomic specificity of various effector cell functions, and underscore the importance of real-time intravital imaging to account for the dynamic behavior of cells as a critical determinant of immunity.

EXPERIMENTAL PROCEDURES

Mice

Specific pathogen-free C57BL/6, B6(Cg)-Tyrc-2J/J (albino B6), and STOCK Tg (CAG-DsRed*MST)1Nagy/J were obtained from The Jackson Laboratory or from Taconic Farms. LysM-eGFP mice (Faust et al., 2000) were acquired through the NIAID Intramural Research Repository and bred in house. STOCK Tg (CAG-DsRed*MST)1Nagy/J were crossed to OT-I TCR transgenic mice (acquired through the NIAID Intramural Research Repository) to create DsRed OT-I mice. Six-sixteen week old adult mice were used in all experiments. All mice were housed under specific pathogen-free conditions (including MNV, MPV, and MHV). All animal procedures were approved by and performed in accordance with the NIAID Animal Care and Use Committee.

Viruses and infections

Mice were infected ec. in the ear pinnae by 10–15 pokes with a bifurcated needle dipped in rVV (stock titer ~ 1×10^8 pfu/ml). VV-NP-S-eGFP has been previously described (Norbury et al., 2002); VV-NP-S-BFP (having blue fluorescent protein instead of green) was constructed according to established protocols (Earl et al., 2001). VV-BFP-Ub-SIINFEKL was constructed to allow liberation of SIINFEKL peptide by cytosolic ubiquitin hydrolase (described in (Fruci et al., 2003)).

Adoptive transfers

$CD8^+$ T cells were purified by negative selection using magnetic-activated cell sorting (MACS) (Miltenyi Biotec). Cells were 90–95% pure by flow cytometry. 2×10^5 dsRed OT-I cells were transferred prior to infection.

Antibody and drug administration

Unless otherwise indicated, mice received 0.5 mg of anti-CD8 (clone 2.43) or GR-1 (clone RB6-8C5), or .25 mg of anti-Ly6g (clone 1A8) alone or together intraperitoneally (ip.) at d0 and every other day thereafter. For analysis of lesion resolution in the absence of T cells, mice were given anti-CD8 (clone 2.43) on day 6, 8, and 10. Antibodies were purchased from BioXcell. AT38 was dissolved in 1% carboxymethylcellulose in sterile saline solution and 0.5 mg injected ip at 4 or 4 and 5 d.p.i. as indicated.

Flow cytometric analyses

Single cell suspensions of ears were prepared by collagenase digestion (Type II, Worthington Biochemicals) and filtration through 70 μm nylon cell strainers. Cells were stained with: CD45 (30-F11), CD8 (53-6.7), CD11c (HL3), CD11b (M1/70), CD103 (2E7), Ly6CG (GR-1, RB6-8C5), Ly6G (1A8), F4/80 (BM/8), and CD45.1 (A20) (eBiosciences). For staining for IFN-γ production, brefeldin A (10 μg/ml, Sigma-Aldrich) was added during collagenase digestion, and cells were incubated an additional 2 hours in BFA-containing RPMI (Life Technologies). Cells were stained for CD8 and CD45.1, fixed with 3.2% paraformaldehyde, and stained with anti-IFN-γ (clone XMG1.2, ebioscience) in 0.5% saponin. Cells were stained for CellRox (Life Technologies) with a 2 h incubation.

Viral titering via plaque assay

Ears were collagenase digested, disrupted by pipetting, freeze-thawed 3X, sonicated 3X, serially diluted and plated on TK^- cells. Cells were incubated for 2 d. and plaques counted.

Cell sorting and plaque analysis

Ears from 5–10 mice/group were dissociated with collagenase, and an aliquot frozen at this point. Cells were filtered and stained for CD45 (30-F11), and sorted (BD FACSaria) into $eGFP^+$ $CD45^+$ and eGFP− $CD45^+$ subsets. Sorted cells and the whole-ear aliquot were titered via plaque assay. PFU from sorted cells were normalized to 3 x 10^5 cells, the average number of infected inflammatory monocytes/ear. Percentage contribution of outliers was calculated as PFU per 3 x 10^5 sorted cells/ total PFU per ear.

Statistics

Significances were calculated by Graphpad (Prism) using an unpaired student's *t* test.

Multiplex protein assay

Ears were homogenized in balanced salt solution, 0.1% BSA, and complete protease inhibitor cocktail (Roche). Samples were analyzed with a FlowCytoMix kit (eBioscience) on a BD LSR II flow cytometer and values calculated using FlowCytomixPro software.

Confocal microscopy of frozen sections

Ears were embedded in OCT medium (Electron Microscopy Sciences) and frozen in dry-ice cooled isopentane. Twenty-micron sections were cut on a Leica cryostat (Leica Microsystems). Sections were fixed in ice cold-acetone for 5 min before blocking with 5% goat or donkey serum, then staining with the following: CD8 (53-6.7), CD11b (M1/70), Ly6CG (RB6-8C5), Ly6G (1A8), nitrotyrosine (polyclonal rabbit, Millipore), keratin 5, 6 or 10 (polyclonal rabbit, Abcam). For chemokine staining and nitrotyrosine/chemokine co-staining, ears were fixed in PLP fixative overnight, cryoprotected in 15% sucrose, sectioned, and stained with the following antibodies: CCL3, CCL4, CCL5 (all goat polyclonal, RND System) followed by detection with donkey anti-goat DyLight 649 and donkey anti-rabbit rhodamine red X (Jackson ImmunoResearch). Sections were incubated with secondary antibodies only as controls, and images acquired using identical PMT and laser settings.

Intravital MPM imaging

MPM imaging was performed essentially as described previously (Hickman et al., 2008). Briefly, images were acquired on an upright Leica SP5 confocal microscope (Leica Microsystems) equipped with two Mai Tai Ti:Sapphire lasers (Spectra Physics) with a 10-Watt pumps. Ears were immobilized and bathed in warm saline and imaged with a 20x dipping objective (NA 1.00). Series were obtained in single mode for eGFP/collagen/dsRed

imaging (900 nm laser). BFP/collagen/eGFP/dsRed imaging was performed in sequential mode (900 nm and 800 nm lasers). Emitted fluorescence was collected with a four-channel non-descanned detector equipped with a 495 dichroic and emission filters of 460/50 nm bandpass and 525/50 nm bandpass; and a 560 nm dichroic with a 610/60 bandpass emission filter. Most movies were acquired using 2x zoom, 3-μm *z*-step (total depth of μ45 m) every 30 sec (or 60 sec sequentially). Side-view images were acquired at 1024x1024 resolution, 1.5 μm z-step, total depth of 80–300 μms.

MPM and confocal image analysis

Maximum intensity projections (MIP) were processed from z-stacks using Imaris (Bitplane). Because both collagen (second harmonic generation) and BFP appear in the blue channel, BFP expression was pseudocolored magenta for clarity. In some cases, eGFP was also pseudocolored magenta for continuity in figures. For tracking cellular movement, images were processed using a gaussian filter, then tracks calculated using the "spot" function of Imaris. Overlays of tracks were generated using Imaris XT function "translate tracks" and pseudocolored according to the average speed of the cell creating the track. Average speeds were calculated using the spot-detection function and the following parameters: autoregressive motion, gapclose 1, 7.5 μm object diameter, 20 μm maximum distance. Following automated analyses, tracks were analyzed individually for erroneous connections. For analysis of infected cell movement, 2 h time-series were collected, and average cell speed over that time was plotted. Cells were classified as motile outliers if their speed was > 4 SDs above speeds for infected keratinocytes. T cells per/lesion were calculated manually after using the "spot" detection function of Imaris to define T cells.

Colocalized voxels of confocal images were calculated using the Imaris "Coloc" module. Ratiometric images were produced in Fiji (Math function) by dividing CCL3 fluorescence intensity by nitrotyrosine fluorescence intensity per voxel. For calculation of CCL3/nitrotyrosine mean fluorescent intensity (MFI), confocal images were collected from areas containing lesions or outlying infected cells with care not to mix areas in images. The CCL3 MFI in the entire image divided by the MFI of the whole image for nitrotyrosine.

Supplementary Material

Refer to Web version on PubMed Central for supplementary material.

Acknowledgments

We think the Comparative Medicine Branch and staff of the Bldg. 33 Vivarium for excellence in animal husbandry. This work was generously supported by the National Institute of Allergy and Infectious Diseases Division of Intramural Research

Abbreviations

B6	C57Bl/6
BFP	tag blue-fluorescent protein
CTL	cytotoxic T lymphocyte
d	day
DCs	dendritic cells
d.p.i	day post-infection
ec	epicutaneous

eGFP	enhanced green fluorescent protein
Lys-M	lysozyme M
μms	micrometers
pfu	plaque-forming units
p.i	post-infection
RNS	reactive nitrogen species
RNS	reactive nitrogen species
ROS	reactive oxygen species
rVV	recombinant vaccinia virus

References

Babior BM. NADPH oxidase. Curr Opin Immunol. 2004; 16:42–47. [PubMed: 14734109]

Bedoui S, Whitney PG, Waithman J, Eidsmo L, Wakim L, Caminschi I, Allan RS, Wojtasiak M, Shortman K, Carbone FR, et al. Cross-presentation of viral and self antigens by skin-derived CD103+ dendritic cells. Nat Immunol. 2009; 10:488–495. [PubMed: 19349986]

Chtanova T, Schaeffer M, Han SJ, van Dooren GG, Nollmann M, Herzmark P, Chan SW, Satija H, Camfield K, Aaron H, et al. Dynamics of neutrophil migration in lymph nodes during infection. Immunity. 2008; 29:487–496. [PubMed: 18718768]

Deshmane SL, Kremlev S, Amini S, Sawaya BE. Monocyte chemoattractant protein-1 (MCP-1): an overview. J Interferon Cytokine Res. 2009; 29:313–326. [PubMed: 19441883]

Earl PL, Moss B, Wyatt LS, Carroll MW. Generation of recombinant vaccinia viruses. Curr Protoc Mol Biol. 2001; Chapter 16(Unit 16):17. [PubMed: 18265124]

Faust N, Varas F, Kelly LM, Heck S, Graf T. Insertion of enhanced green fluorescent protein into the lysozyme gene creates mice with green fluorescent granulocytes and macrophages. Blood. 2000; 96:719–726. [PubMed: 10887140]

Fenner, FHD.; Arita, I.; Jezek, Z.; Ladnyi, I. Smallpox and Its Eradication. World Health Organization; Geneva: 1988. p. 1460

Fischer MA, Davies ML, Reider IE, Heipertz EL, Epler MR, Sei JJ, Ingersoll MA, Rooijen NV, Randolph GJ, Norbury CC. CD11b, Ly6G cells produce type I interferon and exhibit tissue protective properties following peripheral virus infection. PLoS Pathog. 2011; 7:e1002374. [PubMed: 22102816]

Flesch IE, Woo WP, Wang Y, Panchanathan V, Wong YC, La Gruta NL, Cukalac T, Tscharke DC. Altered CD8(+) T cell immunodominance after vaccinia virus infection and the naive repertoire in inbred and F(1) mice. J Immunol. 2010; 184:45–55. [PubMed: 19949110]

Freedberg IM, Tomic-Canic M, Komine M, Blumenberg M. Keratins and the keratinocyte activation cycle. J Invest Dermatol. 2001; 116:633–640. [PubMed: 11348449]

Fruci D, Lauvau G, Saveanu L, Amicosante M, Butler RH, Polack A, Ginhoux F, Lemonnier F, Firat H, van Endert PM. Quantifying recruitment of cytosolic peptides for HLA class I presentation: impact of TAP transport. J Immunol. 2003; 170:2977–2984. [PubMed: 12626550]

Halliwell B. Phagocyte-derived reactive species: salvation or suicide? Trends Biochem Sci. 2006; 31:509–515. [PubMed: 16890439]

Hersperger AR, Siciliano NA, Eisenlohr LC. Comparable Polyfunctionality of Ectromelia Virus- and Vaccinia Virus-Specific Murine T Cells despite Markedly Different In Vivo Replication and Pathogenicity. J Virol. 2012; 86:7298–7309. [PubMed: 22532670]

Hickman HD, Li L, Reynoso GV, Rubin EJ, Skon CN, Mays JW, Gibbs J, Schwartz O, Bennink JR, Yewdell JW. Chemokines control naive CD8+ T cell selection of optimal lymph node antigen presenting cells. J Exp Med. 2011; 208:2511–2524. [PubMed: 22042976]

Hickman HD, Takeda K, Skon CN, Murray FR, Hensley SE, Loomis J, Barber GN, Bennink JR, Yewdell JW. Direct priming of antiviral CD8+ T cells in the peripheral interfollicular region of lymph nodes. Nat Immunol. 2008; 9:155–165. [PubMed: 18193049]

Iannacone M, Moseman EA, Tonti E, Bosurgi L, Junt T, Henrickson SE, Whelan SP, Guidotti LG, von Andrian UH. Subcapsular sinus macrophages prevent CNS invasion on peripheral infection with a neurotropic virus. Nature. 2010; 465:1079–1083. [PubMed: 20577213]

Jiang X, Clark RA, Liu L, Wagers AJ, Fuhlbrigge RC, Kupper TS. Skin infection generates non-migratory memory CD8+ T(RM) cells providing global skin immunity. Nature. 2012; 483:227–231. [PubMed: 22388819]

Junt T, Moseman EA, Iannacone M, Massberg S, Lang PA, Boes M, Fink K, Henrickson SE, Shayakhmetov DM, Di Paolo NC, et al. Subcapsular sinus macrophages in lymph nodes clear lymph-borne viruses and present them to antiviral B cells. Nature. 2007; 450:110–114. [PubMed: 17934446]

Lane HC, Montagne JL, Fauci AS. Bioterrorism: a clear and present danger. Nat Med. 2001; 7:1271–1273. [PubMed: 11726956]

Lev A, Princiotta MF, Zanker D, Takeda K, Gibbs JS, Kumagai C, Waffarn E, Dolan BP, Burgevin A, Van Endert P, et al. Compartmentalized MHC class I antigen processing enhances immunosurveillance by circumventing the law of mass action. Proc Natl Acad Sci U S A. 2010; 107:6964–6969. [PubMed: 20351281]

Li JL, Goh CC, Keeble JL, Qin JS, Roediger B, Jain R, Wang Y, Chew WK, Weninger W, Ng LG. Intravital multiphoton imaging of immune responses in the mouse ear skin. Nat Protoc. 2012; 7:221–234. [PubMed: 22240584]

Lindquist RL, Shakhar G, Dudziak D, Wardemann H, Eisenreich T, Dustin ML, Nussenzweig MC. Visualizing dendritic cell networks in vivo. Nat Immunol. 2004; 5:1243–1250. [PubMed: 15543150]

Liu L, Zhong Q, Tian T, Dubin K, Athale SK, Kupper TS. Epidermal injury and infection during poxvirus immunization is crucial for the generation of highly protective T cell-mediated immunity. Nat Med. 2010; 16:224–227. [PubMed: 20081864]

Molon B, Ugel S, Del Pozzo F, Soldani C, Zilio S, Avella D, De Palma A, Mauri P, Monegal A, Rescigno M, et al. Chemokine nitration prevents intratumoral infiltration of antigen-specific T cells. J Exp Med. 2011; 208:1949–1962. [PubMed: 21930770]

Moss, B. Poxviridae: the viruses and their replication. In: Knipe, DMaH; PM, editors. Fields Virology. Lippincott-Raven; 2001. p. 2849-2884.

Moutaftsi M, Peters B, Pasquetto V, Tscharke DC, Sidney J, Bui HH, Grey H, Sette A. A consensus epitope prediction approach identifies the breadth of murine T(CD8+)-cell responses to vaccinia virus. Nat Biotechnol. 2006; 24:817–819. [PubMed: 16767078]

Moutaftsi M, Salek-Ardakani S, Croft M, Peters B, Sidney J, Grey H, Sette A. Correlates of protection efficacy induced by vaccinia virus-specific CD8+ T-cell epitopes in the murine intranasal challenge model. Eur J Immunol. 2009; 39:717–722. [PubMed: 19224639]

Navarro JM, Casatorres J, Jorcano JL. Elements controlling the expression and induction of the skin hyperproliferation-associated keratin K6. J Biol Chem. 1995; 270:21362–21367. [PubMed: 7545670]

Nolz JC, Harty JT. Strategies and implications for prime-boost vaccination to generate memory CD8 T cells. Adv Exp Med Biol. 2011; 780:69–83. [PubMed: 21842366]

Norbury CC, Malide D, Gibbs JS, Bennink JR, Yewdell JW. Visualizing priming of virus-specific CD8+ T cells by infected dendritic cells in vivo. Nat Immunol. 2002; 3:265–271. [PubMed: 11828323]

Remakus S, Sigal LJ. Gamma interferon and perforin control the strength, but not the hierarchy, of immunodominance of an antiviral CD8+ T cell response. J Virol. 2011; 85:12578–12584. [PubMed: 21917955]

Salek-Ardakani S, Arens R, Flynn R, Sette A, Schoenberger SP, Croft M. Preferential use of B7.2 and not B7.1 in priming of vaccinia virus-specific CD8 T cells. J Immunol. 2009; 182:2909–2918. [PubMed: 19234186]

Seedhom MO, Mathurin KS, Kim SK, Welsh RM. Increased protection from vaccinia virus infection in mice genetically prone to lymphoproliferative disorders. J Virol. 2012; 86:6010–6022. [PubMed: 22438562]

Simon ID, Publicover J, Rose JK. Replication and propagation of attenuated vesicular stomatitis virus vectors in vivo: vector spread correlates with induction of immune responses and persistence of genomic RNA. J Virol. 2007; 81:2078–2082. [PubMed: 17151110]

Sutter G, Moss B. Nonreplicating vaccinia vector efficiently expresses recombinant genes. Proc Natl Acad Sci U S A. 1992; 89:10847–10851. [PubMed: 1438287]

Szabo C, Ischiropoulos H, Radi R. Peroxynitrite: biochemistry, pathophysiology and development of therapeutics. Nat Rev Drug Discov. 2007; 6:662–680. [PubMed: 17667957]

Tscharke DC, Karupiah G, Zhou J, Palmore T, Irvine KR, Haeryfar SM, Williams S, Sidney J, Sette A, Bennink JR, Yewdell JW. Identification of poxvirus CD8+ T cell determinants to enable rational design and characterization of smallpox vaccines. J Exp Med. 2005; 201:95–104. [PubMed: 15623576]

Tscharke DC, Woo WP, Sakala IG, Sidney J, Sette A, Moss DJ, Bennink JR, Karupiah G, Yewdell JW. Poxvirus CD8+ T-cell determinants and cross-reactivity in BALB/c mice. J Virol. 2006; 80:6318–6323. [PubMed: 16775319]

Weiss RA, Eichner R, Sun TT. Monoclonal antibody analysis of keratin expression in epidermal diseases: a 48- and 56-kdalton keratin as molecular markers for hyperproliferative keratinocytes. J Cell Biol. 1984; 98:1397–1406. [PubMed: 6201492]

Werner S, Grose R. Regulation of wound healing by growth factors and cytokines. Physiol Rev. 2003; 83:835–870. [PubMed: 12843410]

Xu R, Johnson AJ, Liggitt D, Bevan MJ. Cellular and humoral immunity against vaccinia virus infection of mice. J Immunol. 2004; 172:6265–6271. [PubMed: 15128815]

Yewdell JW. Confronting complexity: real-world immunodominance in antiviral CD8+ T cell responses. Immunity. 2006; 25:533–543. [PubMed: 17046682]

Yirrell DL, Norval M, Reid HW. Local epidermal viral infections: comparative aspects of vaccinia virus, herpes simplex virus and human papillomavirus in man and orf virus in sheep. FEMS Immunol Med Microbiol. 1994; 8:1–12. [PubMed: 8156048]

Zhao Y, Croft M. Dispensable role for 4-1BB and 4-1BBL in development of vaccinia virus-specific CD8 T cells. Immunol Lett. 2012; 141:220–226. [PubMed: 22037570]

HIGHLIGHTS

- Vaccinia virus infects keratinocytes in epidermal foci and monocytes outlying foci
- $CD8^+$ T cells remain peripheral to foci and mainly kill infected monocytes
- $Ly6G^+$ innate immune cells infiltrate and control virus-infected cells within foci
- $CD8^+$ T cells and $Ly6G^+$ innate immune cells synergize to control infection

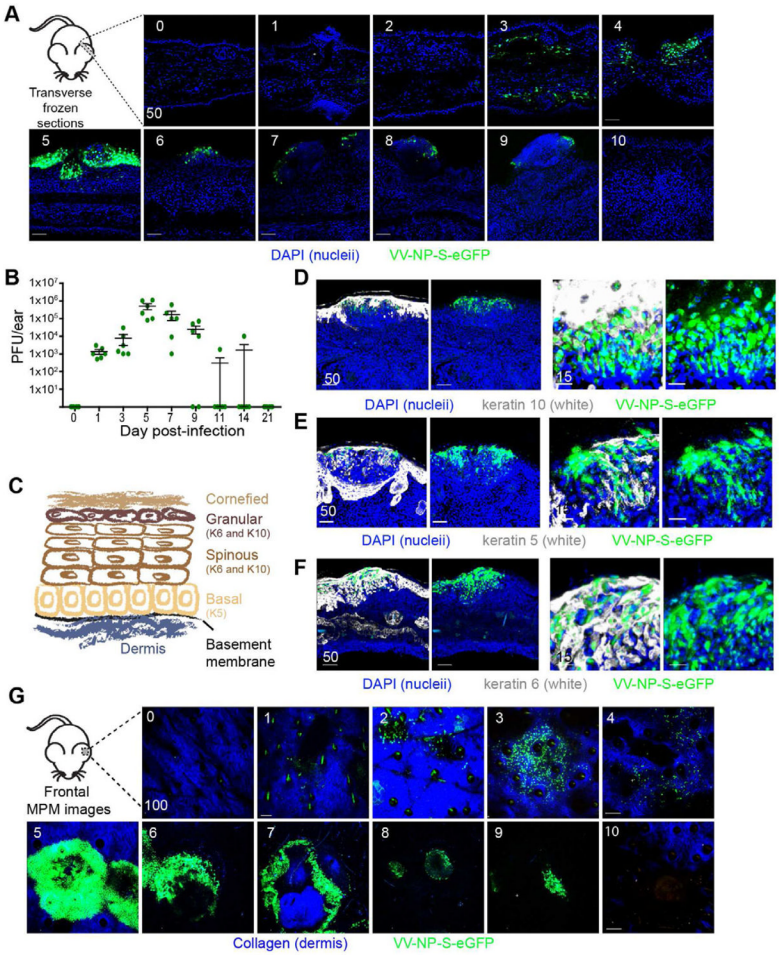

Figure 1. Imaging vaccinia virus infection of the skin

A) Confocal images of transverse ear sections: d.p.i., upper right corner, nuclei=blue (DAPI), green=virus infected cell. **B**) Viral titer/ear determined by plaque assay at indicated d.p.i. Dots represent individual ears. Error bars = SEM **C**) Schematic of skin and representative keratins **D–F**) Confocal images of transverse ear sections taken 5 d.p.i. Keratin 10 (D), 5 (E) or 6 (F) staining=white, nuclei=blue (DAPI), virus-infected cells=green. White staining omitted in the right panels. Higher magnification views shown in the right two panels. **G**) MIPs of MPM images of frontal ear sections. Dermis=blue (SHG), virus-infected cell=green. Scalebars=μms.

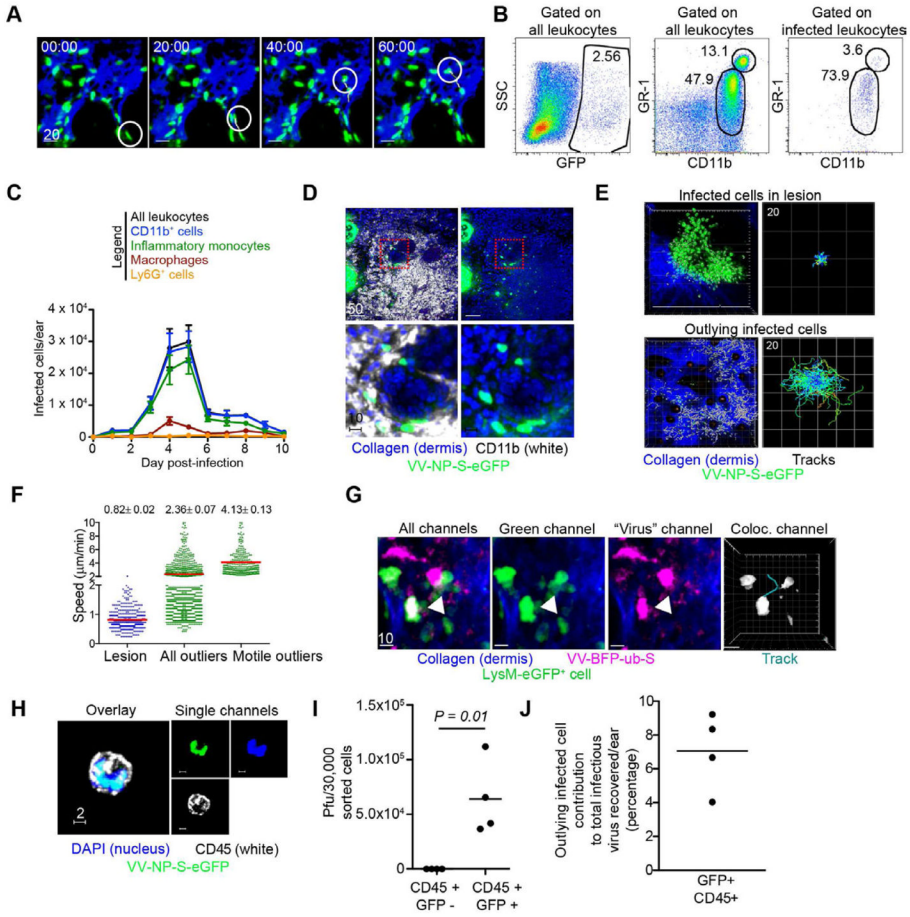

Figure 2. see also Figure S1 and Movie S1. Mobile inflammatory monocytes outlying keratinocytic lesions are infected

A) MPM images of mobile infected cells in the dermis. Virus infected-cell=green, dermis=blue. Time=min. A highly motile cell is circled; track shown in white. **B)** Representative flow dot plots of cells recovered from collagenase-dissociated ears 5 d.p.i. Plots were gated on CD45^{+} leukocytes. Middle panel shows total CD11c^{-} CD11b^{+} GR-1^{int} and ^{hi} cells. Right panel gated only on infected (eGFP^{+}) cells. **C**) Number of each subset of infected cells/ear. N=6 ears/timepoint. Error bars= SEM. **D**) Confocal images of transverse ear sections 5 d.p.i. with VV-NP-S-eGFP (virus=green, nuclei=blue (DAPI), CD11b staining=white). Bottom panels) higher magnification of red dashed boxes. Right panels) no white staining. **E**) MPM images of infected cells in a keratinocytic lesion 5 d.p.i. (top panels) or in outlying cells (bottom panels) over a 2 h period. (virus-infected cells=green, dermis=blue) Right panels) Cell migration tracks of infected cells translated to the same origin. Scale is shown in upper left in μms/box of grid (note grid area is larger for outlying infected cells (bottom)). Tracks classified by mean cell speed (slow (blue) to fast (red)). **F**) Mean cellular speed within lesion (blue dots), outlying lesion (green dots), or those >4 SD from speeds of those in lesion (green dots, right). Average speeds and SEM shown. **G**) MPM images of a LysM-eGFP mouse infected with VV-BFP-Ub-S (pseudocolored magenta). Colocation of green/magenta is shown in white. Cell migration track (right panel). Scalebars=μms. **H**) Confocal image of a sorted eGFP+ CD45+ cell as overlay (left panel) or individual channels (right panels). CD45=white, VV-NP-S-eGFP=green, nuclei=blue. **I**) Viral titers from sorted, infected (eGFP+) or uninfected (eGFP−) CD45^{+} cells 5 d.p.i., normalized to average number of infected cells recovered per ear. **J**) Contribution of

outlying infected cells to total infectious virus 5 d.p.i. Each experiment was repeated 3–4 times with 3–10 mice/group. Scalebars=μms

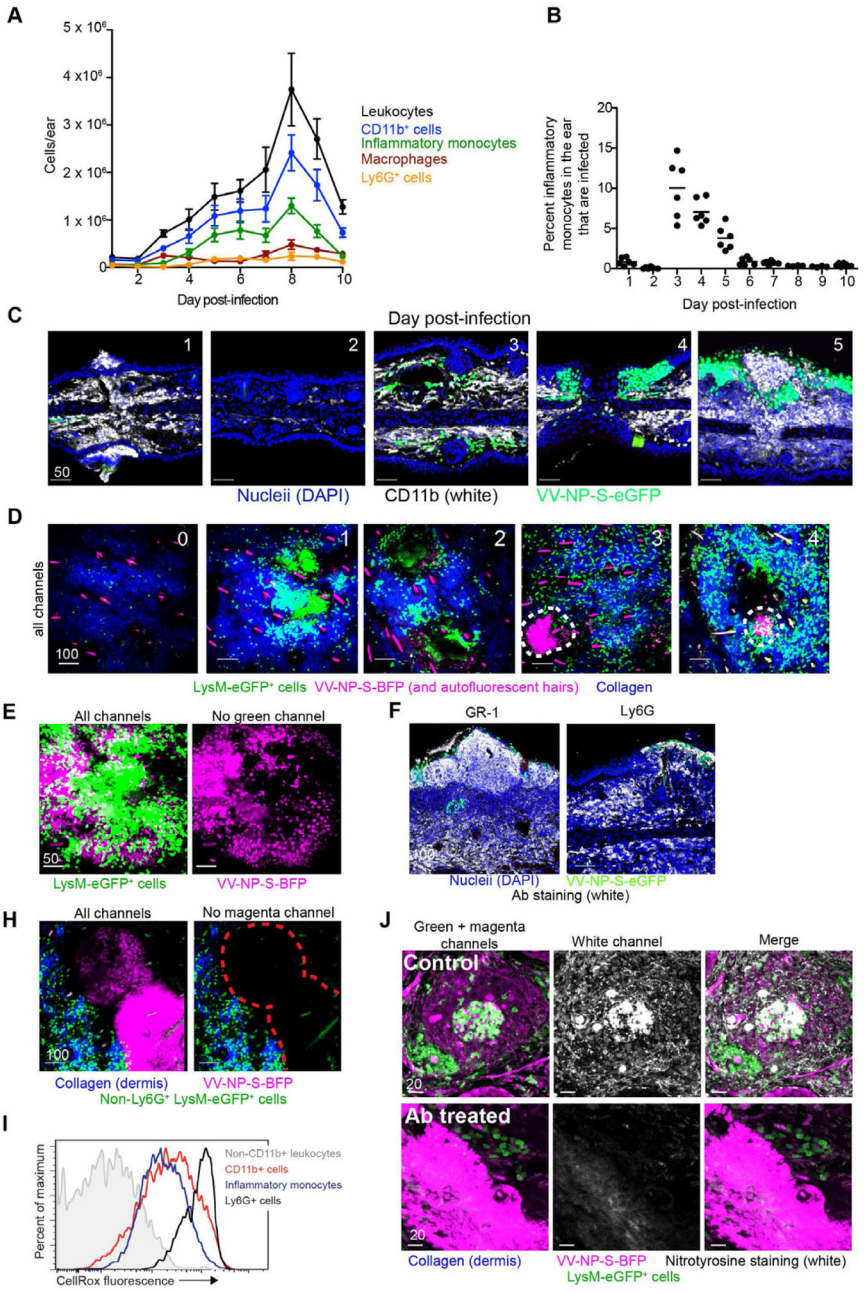

Figure 3. see also Movie S2. Innate cells immigrate into tissue and infiltrate keratinocytic lesions

A) Number of subsets of $CD11b^+$ cells per d.p.i. N=6 ears/timepoint. Error bars= SEM **B**) Percent of total $CD11b^+$ $GR\text{-}1^{int}$ $Ly6G^-$ $F4/80^-$ $CD11c^-$ cells infected with VV (expressing eGFP) at each d.p.i. Line=mean. Dots=individual ears. **C**) Confocal images of transverse ear sections. CD11b=white, nucleii=blue, virus-infected cell=green. d.p.i.=upper left corner. **D**) MIPs of MPM images (frontal sections) of LysM-eGFP mice (green macrophages, monocytes, and neutrophils) infected with VV-NP-S-BFP (pseudocolored magenta). Dermis=blue. Red dashed lines highlight lesions. d.p.i.=upper left corner. **E**) Higher magnification images of LysM-eGFP 5 d.p.i. Right panel) only infected cells (magenta). **F**) Transverse ear section 5 d.p.i. with NP-S-eGFP (green), stained for with GR-1 (Ly6CG, left)

or LY6G (right). Staining=white, DAPI=blue. **H)** MIP of MPM images of LysM-eGFP mice 5 d.p.i. with VV-NP-S-BFP (pseudocolored magenta) after anti-Ly6G Ab depletion. **I**) Flow cytometric histograms showing CellRox fluorescence (ROS indicator) by each cell subset. **J**) Frozen sections from LysM-eGFP mice 5 d.p.i. with VV-NP-S-BFP (pseudocolored magenta) stained for nitrotyrosine (white). Top panels=control mice, bottom panels=anti-Ly6CG-depleted mice. White channel alone (middle). Confocal images were repeated twice. Other experiments were repeated 3–4 times with 3–4 mice/group. Scalebars=μms.

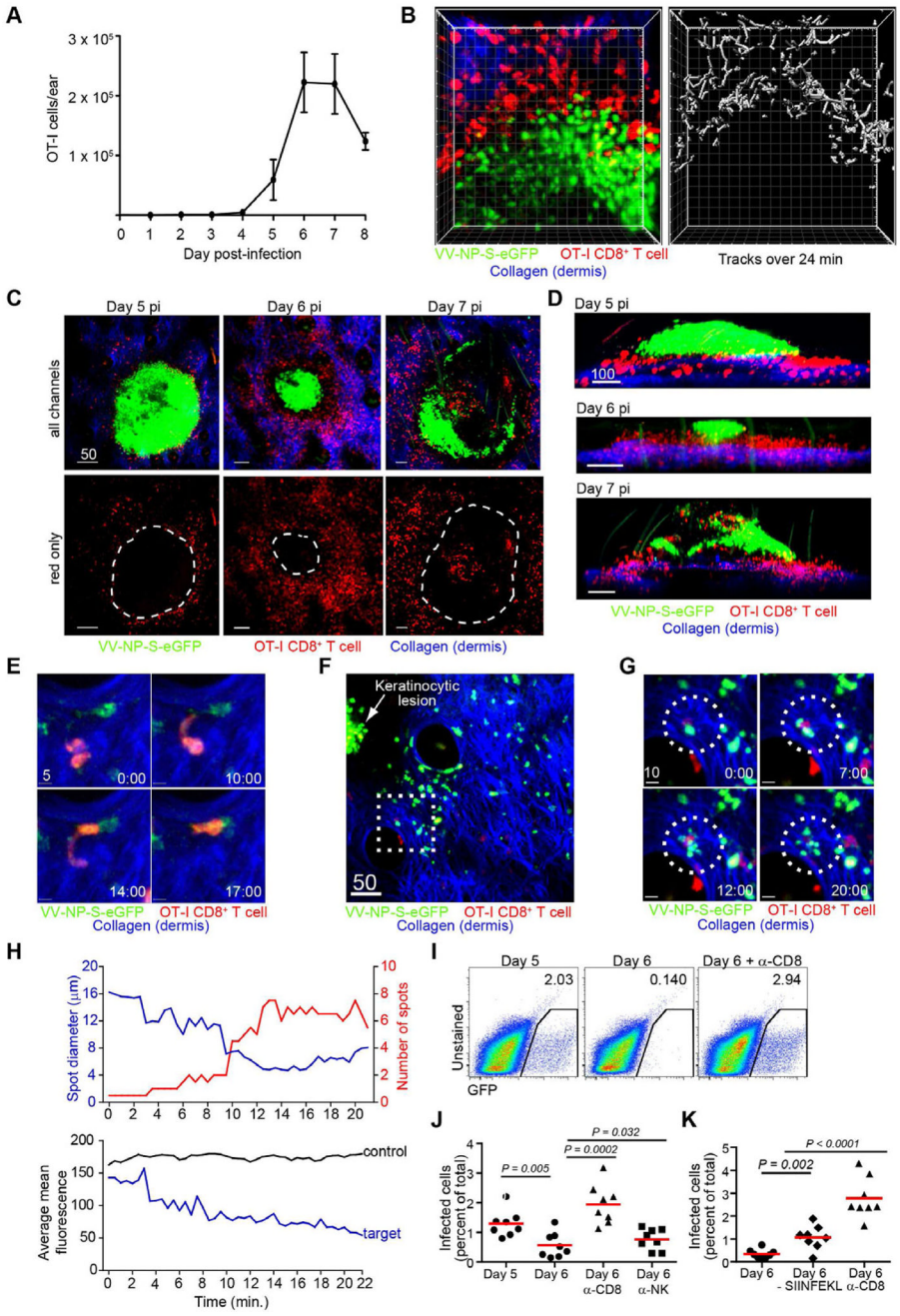

Figure 4. see also Figure S2 and Movie S3. CD8$^+$ T cells are excluded from lesions but eliminate peripheral infected inflammatory monocytes

A) OT-I CD8$^+$ T cells in ear after VV-NP-S-eGFP infection. 2x10^5 dsRed OT-I CD8$^+$ T cells were adoptively transferred prior to infection. Error bars=SEM. n=8 ears/d.p.i. **B)** MIP MPM images of OT-I CD8$^+$ T cells (red) at the border of a keratinocytic lesion (green). Dermis=blue. Tracks of T cells over a 24 min. (right panel). Individual boxes=10 μms **C**) MIP MPM images. OT-I CD8$^+$ T cells=red, virus-infected cell=green. Bottom panels) only CD8$^+$ T cells with lesion location outlined (dashed lines). **D**) Side views of MIP MPM images showing T cell (red) location relative to keratinocytic lesion (green). **E**) MIP MPM images of an OT-I cell (red) squeezing through the dermis (collagen (blue)) to interact with

a VV-NP-S-eGFP-infected cell (green). **F**) MIP MPM image of OT-I $CD8^+$ T cells (red) outlying a keratinocytic lesion (green, indicated with a white arrow). Dashed box shown in higher magnification. **G**) MPM images of a T cell killing of a VV-infected cell. time (min)=lower right. Dashed circle highlights interaction. **H**) Spot calculations of target cell. top panel) number of spots detected (red) compared to the average diameter of spots (blue). bottom panel) mean fluorescence of all spots (blue) compared to a non-target control. **I**) Flow cytometric plots of GFP^+ infected cells recovered 5 (left) or 6 (middle) d.p.i. Right=plot 6 d.p.i. with CD8-depleting Ab throughout infection. Numbers indicate percentage of $eGFP^+$ leukocytes recovered. **J**) Chart=individual ears from mice on 5 d.p.i. (dots, left), 6 d.p.i. (dots, middle left), 6 d.p.i. with anti-CD8 (triangles), or 6 d.p.i. with anti-NK1.1 (squares). Lines show means. **K**) as in J) but with mice infected with a virus lacking SIINFEKL (middle diamonds and triangles) compared to one expressing cognate antigen for OT-I cells (circles). Flow experiments were performed at least 3 times with 3–5 mice/group. Statistics=student's t test. MPM imaging experiments were performed at least 6 times with 2–5 mice/group. Scalebars=μms.

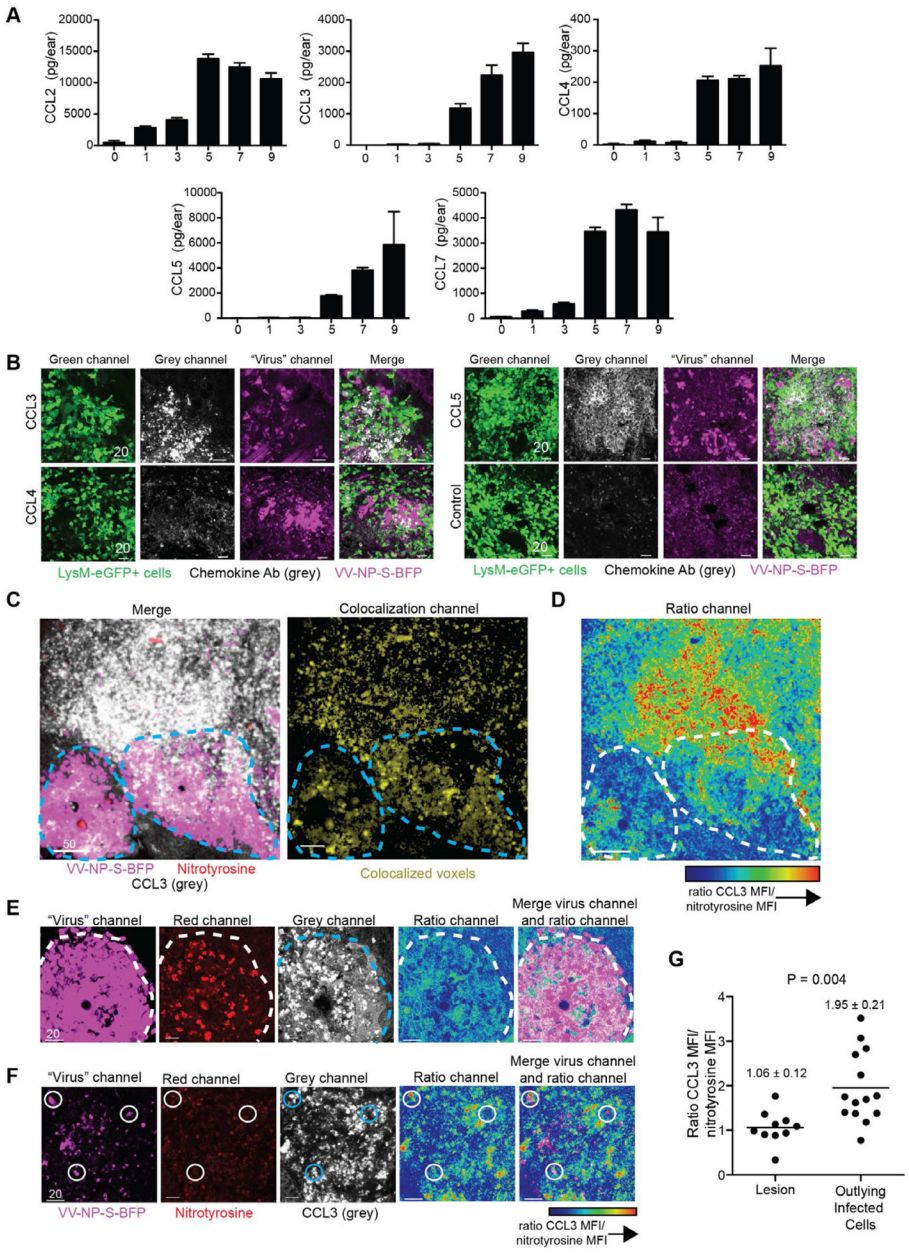

Figure 5. Chemokines induced by VV-infection localize to viral lesion and sites of protein nitration

A) Protein levels of chemokines at indicated d.p.i. (x axis) as determined by multiplex protein assay. Scalebar=SEM. Multiplex experiments were performed 3 times with 3–6 mice/group. **B**) Confocal images of frozen sections from LysM-eGFP mice 5 d.p.i. with VV-NP-S-BFP (pseudocolored magenta) stained for different chemokines (grey). Ab chemokine specificity is indicated on left panel. Control = secondary Ab staining alone. **C**) left panel) Confocal image of a frozen section (WT mouse) 5 d.p.i. with VV-NP-S-BFP (pseudocolored magenta) stained for nitrotyrosine (red) and CCL3 (grey). Right panel) Colocalization of nitrotyrosine and CCL3 staining (yellow). Lesion borders=dashed lines. **D**) Ratiometric image of CCL3 staining/nitrotyrosine staining. Highest ratio of CCL3 to nitrotyrosine is indicated by red coloring as shown in scalebar. Lesion borders=dashed lines. **E**) Higher

magnification image of a lesion (pseudocolored magenta) 5 d.p.i. stained for nitrotyrosine (red) and CCL3 (grey). Ratio images (right). Lesion borders=dashed lines. **F**) as in E) but showing region of outlying infected inflammatory monocytes. Infected cell (magenta) surrounded by areas of high CCL3 to nitrotyrosine ratios highlighted by circles. **G**) Numerical calculation of ratio of CCL3 to nitrotyrosine MFI in regions of lesions or outlying infected inflammatory monocytes. Mean and SEM are shown. Statistics = student's t test. Scalebars = μms. Confocal imaging experiments were performed twice with n= 6/ group.

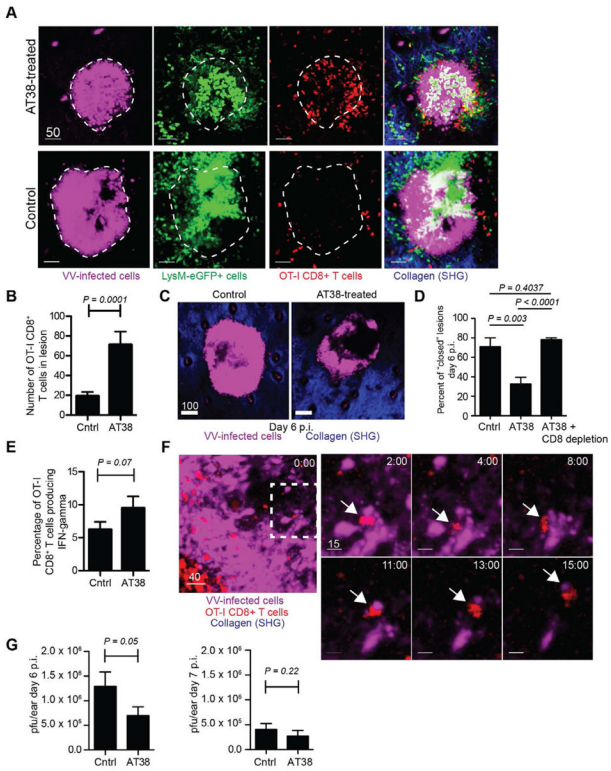

Figure 6. see also Figure S3 and Movie S4. Peroxynitrite blockade relocates T cells into keratinocytic lesions

A) MPM MIP images of LysM-eGFP mice 5 d.p.i. with VV-NP-S-BFP (magenta). $CD8^+$ T cells (red) were imaged with (top panels) and without (bottom panels) AT38 treatment. Imaging depth was limited to lesion depth (i.e. beneath lesion is not shown). **B**) T cells per lesion +/− AT38 as determined by MPM. Results were summed from lesions in 4 mice/group. **C**) MPM images of ears 6 d.p.i. +/− AT38. Lesions=magenta. Dermis=blue. **D**) Percent of lesions that are closed (e.g. no non-fluorescent center) on 6 d.p.i. +/− AT38 determined microscopically. Far column=CD8-depleted, AT38-treated mice. **E**) Percentage of IFN-γ producing OT-I cells +/− AT38 6 d.p.i. **F**) MPM image within a VV-NP-S-BFP lesion (magenta) 5 d.p.i. OT-I CD8+ T cells=red. Dashed box=higher magnification (right). Right panels) T cell carrying off a piece of infected keratinocyte. Arrow highlights interaction. Time (min)=upper right. **G**) Viral titers on 6 and 7 d.p.i. +/− AT38. Experiments were repeated at least 3 times with 3–6 mice/group. Error bars=SEM. Statistics=student's t test. Scalebars=μms.

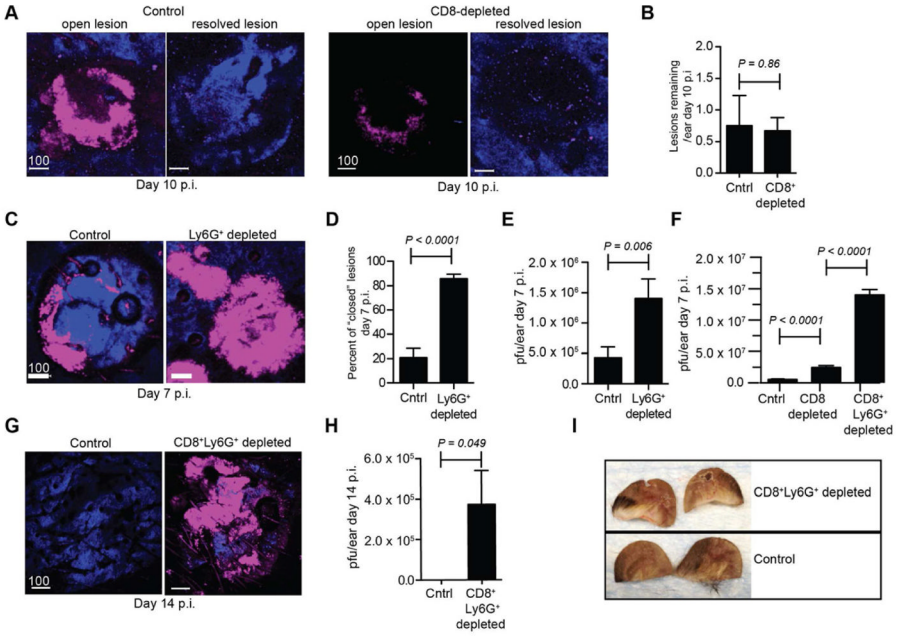

Figure 7. CD8$^+$ T cells and Ly6G$^+$ cells exert coordinated control of peripheral virus infection

A) MPM images 10 d.p.i. in control (left panels) or CD8-depleted (right panels) mice. Mice were given CD8-antibody beginning on day 6. Lesions=magenta, dermis=blue. **B**) Number of lesions/ear 10 d.p.i. in control and CD8-depleted mice. **C**) MPM images 7 d.p.i. +/− anti-Ly6G antibody. Lesions=magenta, dermis=blue. **D–E**) ercent of lesions that are closed (e.g. no non-fluorescent center) (D) or viral titers (E) 7 d.p.i. with Ly6G depletion. **F**) Viral titers 7 d.p.i. with depletion of CD8 alone (middle) or in conjunction with Ly6G-depletion (right). **G–I**) MPM images (G) 14 d.p.i., viral titers (H), and photographic images (I) with continuous depletion of CD8$^+$ T and Ly6G$^+$ cells. Experiments A–F were repeated at least 3 times with 3–6 mice/group. Experiments G–I were repeated twice with 5 mice/group. Scalebar=μms. Statistics=student's t test. Error bars=SEM.